PAPER

Graphene-loaded tin oxide nanofibers: optimization and sensing performance

To cite this article: Zain Ul Abideen *et al* 2017 *Nanotechnology* **28** 035501

View the article online for updates and enhancements.

Graphene-loaded tin oxide nanofibers: optimization and sensing performance

Zain Ul Abideen[1], **Jae Young Park**[2], **Hyoun Woo Kim**[3,4,5] **and Sang Sub Kim**[1,5]

[1] Department of Materials Science and Engineering, Inha University, Incheon 402-751, Korea
[2] Surface R&D Group, Korea Institute of Industrial Technology (KITECH), Incheon 21999, Korea
[3] Division of Materials Science and Engineering, Hanyang University, Seoul 133-791, Korea
[4] The Research Institute of Industrial Science, Hanyang University, Seoul 133-791, Korea

E-mail: hyounwoo@hanyang.ac.kr and sangsub@inha.ac.kr

Abstract

We investigated the gas sensing characteristics of graphene nanosheet (NS)-loaded SnO_2 nanofibers (NFs) that were synthesized by a low-cost facile electrospinning process. The sensing performance was characterized as a function of the graphene content with various gases such as C_6H_6, C_7H_8, CO, CO_2, and H_2S. The loading of graphene NSs significantly improved the gas sensing performances of SnO_2 NFs. The optimal amount of graphene NSs was found to be 0.5 wt%. We proposed a sensing mechanism for the enhanced sensing performance based on the chemical sensitization of graphene NSs and the charge transfer through the heterointerfaces between graphene NSs and SnO_2 nanograins. The results show that graphene NS-loaded SnO_2 NFs are a promising sensing material system that can detect hazardous gaseous species.

S Online supplementary data available from stacks.iop.org/NANO/28/035501/mmedia

Keywords: SnO_2, graphene, H_2S, gas sensor

(Some figures may appear in colour only in the online journal)

1. Introduction

Tin dioxide (SnO_2) was intensively studied for gas sensing applications because of its good chemical and thermal stability, high carrier density, and good detecting abilities to various toxic gases and organic vapors. Moreover, its stability at higher temperatures makes it possible to use SnO_2 in harsh environments where explosive gases might exist. Therefore, much of the research in the field of gas-sensors still focuses on methods to further enhance the sensitivity and selectivity of SnO_2-based gas sensors. This is typically done by controlling the nanostructure morphology and incorporating various additive materials.

Since the morphology and surface state play a significant role in changing the characteristics of sensing materials, different nanostructural configurations and surface morphologies have been studied in attempts to meet the high sensitivity

requirements [1–3]. In this regard, one-dimensional SnO_2 nanostructures, such as nanowires, nanotubes, nanofibers (NFs), nanobelts, and nanorods have shown outstanding chemical sensing performances relative to their bulk counterparts. This difference in performance is caused by the specific matetials properties of the nanostructures, which are generally influenced by the high specific surface area and confined directional carrier support. NFs synthesized by an electrospinning possess an additional unique feature of a web-like morphology, which enables gas molecules to readily interact with and diffuse effectively into all the NFs simultaneously. This enhances the reaction speed and sensitivity. Moreover, the presence of nanograins in the NFs provides additional reaction sites and resistance modulation at grain boundaries. Therefore, SnO_2 NFs are promising for gas sensing materials [4–7].

One of the other commonly and widely employed techniques used to enhance the sensitivity or selectivity is the incorporation of effective additive materials into the sensing

[5] Authors to whom any correspondence should be addressed.

host material. In this regard, many types of additives, including noble metals, transition metals, semiconducting or semimetal elements, light elements, rare-earth elements, and organic materials, have been included in SnO_2 hosts and have been extensively studied for the sensing of various oxidizing and reducing gases [8–13].

Among these, graphitic nanocarbons (particularly graphene) have recently attracted extraordinary attention in the gas sensor community because of their unique properties [14–19]. This structure provides a large specific surface area ($2630 \, m^2 \, g^{-1}$) [20, 21]. All atoms of graphene are essentially surface atoms that are readily exposed to the target gas. Furthermore, graphene has high thermal stability, excellent electrical conductivity, good mechanical strength, high charge carrier mobility, and extremely low electrical noise. As a result, a small quantity of electrons can produce a significant variation in the conductance of graphene [22]. All these characteristics make graphene an attractive material for gas sensing applications [23–25]. Although graphene-based sensors have been used to detect poisonous and explosive gases [26–28], graphene/SnO_2 composites [13] have rarely been investigated. In particular, the effect of graphene loading into nanofibers (NFs) has not been investigated yet.

In this study, we explore the enhanced sensing performances of SnO_2 NFs loaded with graphene NSs for the first time. The SnO_2-graphene-related materials (i.e. graphene or reduced graphene oxide (RGO)) nanocomposites were prepared by a variety of methods (table S1, supporting information). However, there are only a few papers from the authors of the present paper, reporting the preparation in conjunction with the nanofibers. Furthermore, in the present work, we used the graphene instead of RGO, which is different from other RGO/SnO_2 NFs-comprising papers. We also discuss the sensing mechanisms responsible for the enhanced sensing performance realized by adding the graphene NSs.

2. Experimental details

2.1. Materials

Tin(II) chloride dehydrate ($SnCl_2 \cdot 2H_2O$), polyvinyl acetate (PVAc, Mw = 850 000), ethanol (anhydrous, 99.5%), dimethylformamide (DMF, 99.8%), graphene, and de-ionized water were used. All materials were purchased from Sigma-Aldrich Corp. and were used without additional refining.

2.2. Synthesis and characterization of graphene

Expandable graphite (1 g, Hyundai Coma Industry) was put into an alumina crucible. The reaction products were irradiated by rapid microwave heating for 1 min with a frequency of 60 Hz and a power of 1000 W. The exfoliated graphite was sonicated in ethanol for 10 min and was subsequently dried in a vacuum oven. The sonication and drying processes were repeated three times to obtain graphene flakes that consisted of a few layers. More details about the synthesis and characterization procedures that were used in the present study

can be found in our previous reports [29, 30]. In the preparation of few-layer graphene, they were irreversibly intercalated to ensure decoupling. Accordingly, it is surmised that the graphite and the few-layer graphene exfoliated from them will be in the mechanically decoupled configuration. However, the few-layer graphene will be expected to be electrically connected (i.e. not insulated) to the surrounding SnO_2 matrix, because the electronic transport across the graphene/SnO_2 enhances the sensing behavior.

2.3. Synthesis of graphene NS-loaded SnO_2 NFs

Graphene NS-loaded SnO_2 NFs were synthesized using electrospinning. The process is very similar to the previous work [19]. First, PVAc was dissolved by a solvent with equal amounts of ethanol and DMF, and this mixture was continuously stirred for 4 h. Subsequently, $SnCl_2 \cdot 2H_2O$ and the graphene solution were added to the PVAc solution and were stirred continuously for 12 h without heating. The solution was put into a syringe [19]. All the electrospinning experiments were performed at room temperature in air. The NFs were collected on SiO_2-deposited (thickness $\sim$ 250 nm) Si wafers. The prepared electrospun NFs were calcined at 600 °C in air for 30 min at 5 °C min^{-1}. The same procedure was adopted to synthesize the graphene NS-loaded SnO_2 NFs with different graphene concentrations (0.05, 0.1, 0.3, 0.5, 1, and 1.5 wt%). Further details of the procedure used to synthesize electrospun SnO_2 NFs are provided in our earlier report [31]. Previous studies indicate that the RGO is stable at -10 °C–800 °C [32, 33]. Accordingly, the graphene in the present work, which is an RGO with the very small amount of oxygen, will be stable not only during the sensing temperature of 300 °C, but also during the calcination process at 600 °C. Furthermore, we carried out the TGA test, in which no significant weight loss was observed up to 900 °C, in case of pure RGO NSs [12].

2.4. Microstructural and sensing characterization

For microstructural characterization, we used scanning electron microcopy (SEM, Hitachi S-4200) and high-resolution transmission electron microscopy (HR-TEM, Phillips CM-200). To investigate the sensing behavior of graphene NSs-loaded SnO_2 NFs, double layer electrodes of Ti (thickness $\sim$ 50 nm) and Pt (thickness $\sim$ 200 nm) were deposited by the radio frequency magnetron sputtering at room temperature. The complete procedures used for the synthesis of graphene NS-loaded SnO_2 NFs using electrospinning and the fabrication of sensing devices are shown in figure 1. The gas sensing properties of the graphene NS-loaded SnO_2 NFs sensors towards various reducing gases (CO, C_7H_8, C_6H_6, CO_2, and H_2S) at concentrations ranging from 1–5 ppm were measured under atmospheric conditions at an operating temperature between 200 °C and 400 °C. The sensors were placed and evaluated in a testing chamber at constant temperature. Details of sensor design, gas dilution, and the sensing system are provided in our earlier reports [34, 35]. The sensors were stabilized for $\sim$20 min in the baseline gas (synthetic dry air) to obtain a stable resistance at every operating temperature (prior to the gas sensing tests).
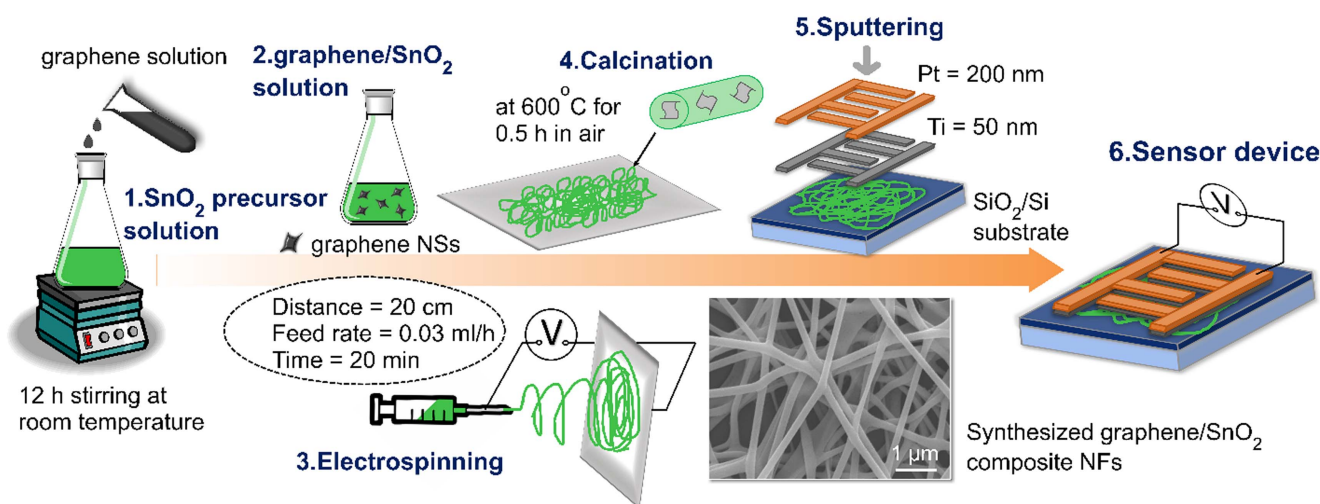
Figure 1. Schematic illustration of the preparation of graphene NSs-loaded SnO$_2$ NFs with the electrospinning process.

The response of the sensors to the reducing gas is defined as the ratio of R_a to R_g. Here, R_a is the original base resistance of the sensor in air, and R_g is the stabilized resistance of the sensor in the presence of the applied gas. The response time (τ_{res}) corresponds to the time in which the resistance of the sensor changes to 90% of the original base resistance, and the recovery time (τ_{rec}) is the required time for the recovery of 90% of the signal.

3. Results and discussion

Figures 2(a)–(f) show the typical microstructures of the calcined graphene NS-loaded SnO$_2$ NFs containing various amounts of graphene NSs. The average diameter of the NFs is estimated to be 200–300 nm, and the lengths are in the range of several micrometers. However, the size of the nanograins and/or the diameter of the NFs were not significantly affected by varying the graphene content. The presence of nanograins on the NFs can be clearly seen. These nanograins evolved during the calcination process. The upper-right insets show that the NFs were uniformly and randomly distributed on the SiO$_2$/Si substrates. The polycrystalline nature of SnO$_2$ NFs (figure 3(a)) and the presence of graphene NSs (figures 3(b) and (c)) were confirmed by HR-TEM. Figures 3(b) and (c) show the presence of graphene sheets along with the nanograins of the NFs. As shown, NFs were anchored and dispersed on the larger graphene NSs (figure 3(b)), while some of the graphene sheets were folded in between the nanograins of the NFs (figure 3(c)). These results confirmed the multilayer graphene configuration. Understanding these kinds of interactions between graphene NSs and SnO$_2$ NFs is important to understand the electrical transport properties and sensing mechanism of graphene NS-loaded SnO$_2$ NFs; this will be discussed in the following paragraphs. The inter-planar distance of the SnO$_2$ NFs was 0.33 nm, which corresponds to the (110) crystallographic plane of the rutile SnO$_2$ phase. Figure 3(d) shows the selected area diffraction ring patterns of graphene NS-loaded SnO$_2$ NFs. These can be indexed to the rutile SnO$_2$ structure (JCPDS Card No. 41-1445). The weakness and invisibility of graphene-related patterns is associated with the low graphene content. However, it is possible that there is a ring pattern that could be indexed to the (002) plane of 2H graphite (JCPDS Card No. 75-1621), which overlaps with the (110) plane of the rutile SnO$_2$ structure. For comparison, a TEM image of pure graphene (without SnO$_2$ NFs) is provided in figures 3(e) and (f). Based on figure 3, we concluded that we successfully synthesized graphene NS-loaded SnO$_2$ NFs.

To investigate the effect of the operating temperature, the graphene NSs-loaded SnO$_2$ NFs and pristine SnO$_2$ NFs were exposed to C$_7$H$_8$ gas at various temperatures (200, 250, 300, 325, 350, 375, and 400 °C) (figure 4(a)). Figure 4(b) shows the responses of pristine SnO$_2$ and graphene NS-loaded SnO$_2$ NFs to 1 ppm of C$_7$H$_8$ gas at different temperatures. The responses of the graphene NS-loaded SnO$_2$ NFs were significantly higher than the pristine SnO$_2$ NFs for all temperatures. It is also clear that graphene NSs-loaded SnO$_2$ NFs showed an increased response at lower temperatures with a maximum response of 3.13 at 300 °C. The response became less sensitive at higher temperatures. In contrast to graphene NS-loaded SnO$_2$ NFs, pristine SnO$_2$ NFs showed a maximum response of 1.94 at 325 °C. The response of the graphene/SnO$_2$ NFs was 76.8% higher than that of the pristine SnO$_2$ NFs at their respective optimal temperatures. The responses of both pristine SnO$_2$ and graphene NS-loaded SnO$_2$ NFs exhibited a bell-shaped behavior, which is consistent with the literature. This trend, which possessed a volcano shape, was observed to increase in height and shift towards lower temperatures when the semiconductor materials were loaded with catalyst materials (e.g., transition metal, graphene, etc). Similar trends were also reported elsewhere [13, 36–39], for SnO$_2$ for H$_2$ gas [37], CdIn$_2$O$_3$ nanocrystals for ethanol gas [38], and Au-functionalized reduced graphene oxide-loaded SnO$_2$ nanofibers for CO gas [39]. We expected that chemical reactions will be deactivated at low temperatures, whereas adsorption will be suppressed at temperatures that are too high [40, 41].
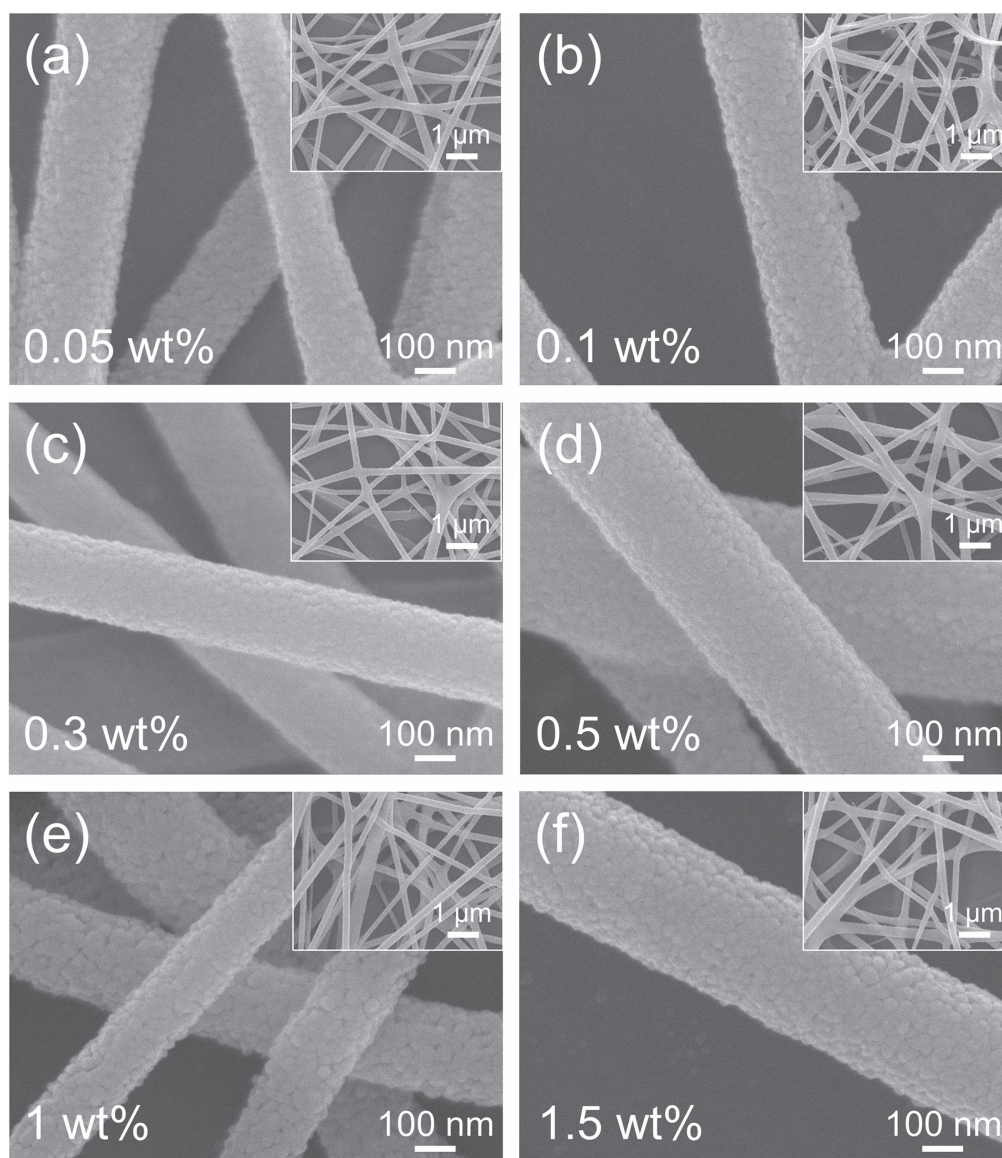
Figure 2. SEM images of the synthesized graphene NSs-loaded SnO$_2$ NFs with the graphene content of (a) 0.05, (b) 0.1, (c) 0.3, (d) 0.5, (e) 1, and (f) 1.5 wt% (upper-right insets: low resolution SEM images).

To examine and compare the sensing properties of graphene NS-loaded SnO$_2$ NFs with pristine SnO$_2$ NFs, we first exposed the sensors to trace concentrations (1, 3, and 5 ppm) of a relatively weak reducing gas (C$_7$H$_8$) at the optimal temperature of 300 °C. This was done to investigate the effect of loading graphene and to select the optimal amount of graphene NSs in the SnO$_2$ NFs needed to obtain the maximum response (as compared to the rest of the sensors). The dynamic resistance curves of the pristine SnO$_2$ and graphene NSs-loaded SnO$_2$ NFs containing various amounts of graphene (0.05, 0.1, 0.3, 0.5, 1, and 1.5 wt%) are shown as a function of the gas concentration in figure 5(a). The resistance of the sensors decreased upon exposure to the C$_7$H$_8$ and returned to its base resistance upon removal of the gas. The sensing behavior of the graphene NS-loaded SnO$_2$ NFs was similar to that of a typical n-type material-based gas sensor (i.e., a decrease was observed in the resistance upon introduction of a reducing gas). This suggests that the electrical

conductivity mainly occurred through the n-type SnO$_2$ semiconducting oxide as opposed to the p-type graphene NSs. This is likely caused by the low content of graphene. The responses of all the sensors to C$_7$H$_8$ gas at 300 °C are shown in figure 5(b). The response of the sensors increased as the gas concentration increased. It is also clear that the SnO$_2$ NF-containing graphene was more sensitive to trace concentrations of the gas compared to pristine SnO$_2$ NFs at the same operating temperature. However, the optimal amount of graphene was observed to be 0.5 wt% with the highest response of 3.13 and a very short response time of 51.2 s as compared to the rest of the sensors (at 1 ppm of C$_7$H$_8$ gas at 300 °C; figures 5(c) and (d)). In contrast, the response of pristine SnO$_2$ NFs was 1.7 with a response time of 125 s. The response of graphene NS-loaded SnO$_2$ NFs increased by 84.1% and had an improved response time relative to SnO$_2$ NFs. The response and recovery times of all sensors to 1 ppm of C$_7$H$_8$ are shown in figure 5(d). The shortest response time was
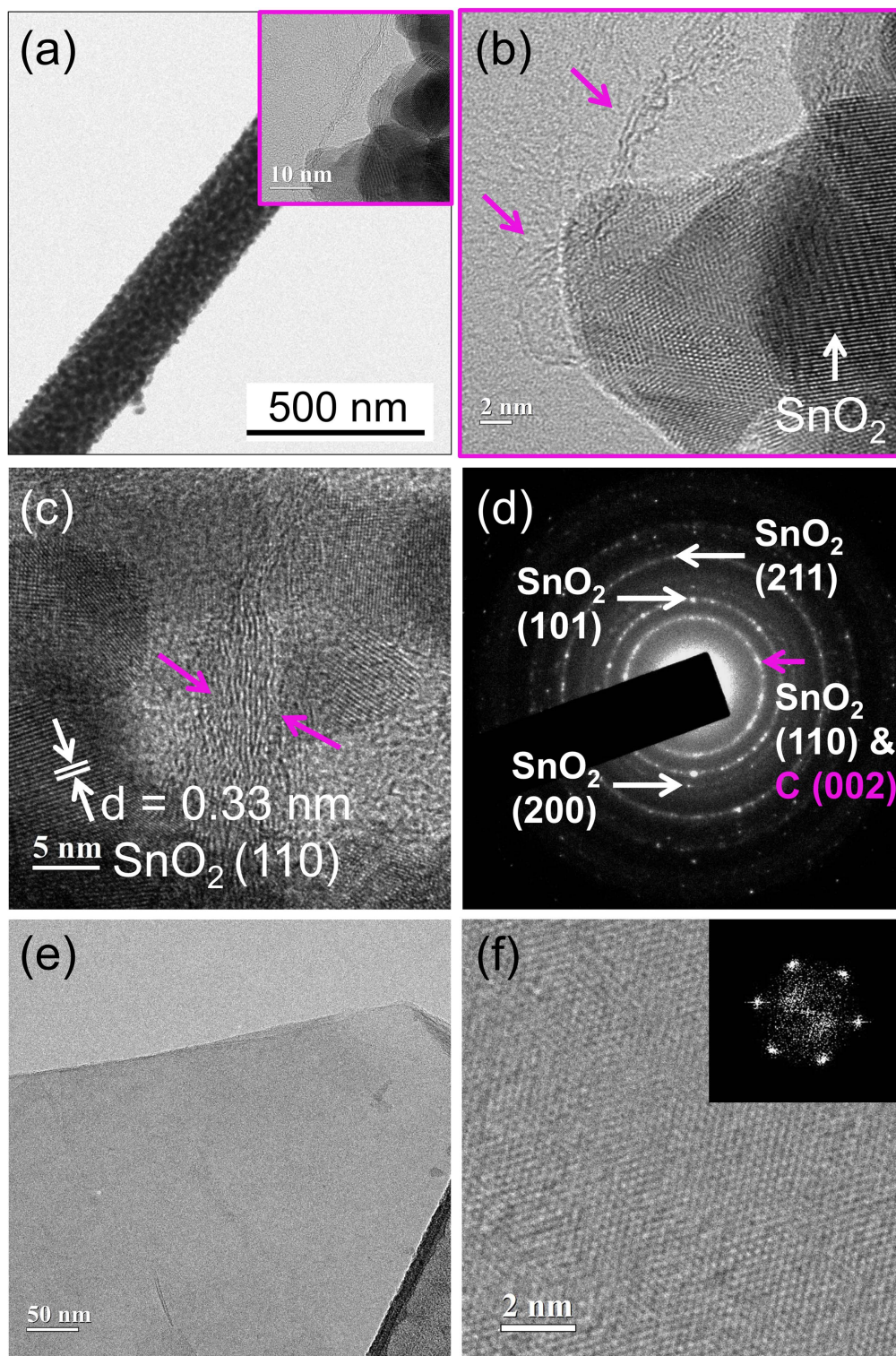
Figure 3. (a) TEM mage of a graphene NSs-loaded SnO₂ NFs. (b) Enlarged HR-TEM image. (c) Lattice-resolved HR-TEM image. (d) Corresponding SAED pattern. (e) Low-magnification TEM image and (f) lattice-resolved TEM image of the pure graphene (inset: associated FFT pattern).

obtained by inserting 0.5 wt% graphene. However, the response of the sensors decreased significantly for concentrations higher than 0.5 wt% graphene. All the remaining sensing experiments were carried out with sensors containing the optimized amount of graphene (0.5 wt%). The bell-shaped response behavior as a function of the graphene concentration

is discussed below after we establish the sensing mechanism of graphene NS-loaded SnO₂ NFs.

To investigate the selectivity and the effect of interfering gases, graphene NS-loaded SnO₂ NFs were tested for other reducing and toxic gases, such as C_6H_6, C_7H_8, CO, CO_2, and H_2S, at the optimal operating temperature. The gas
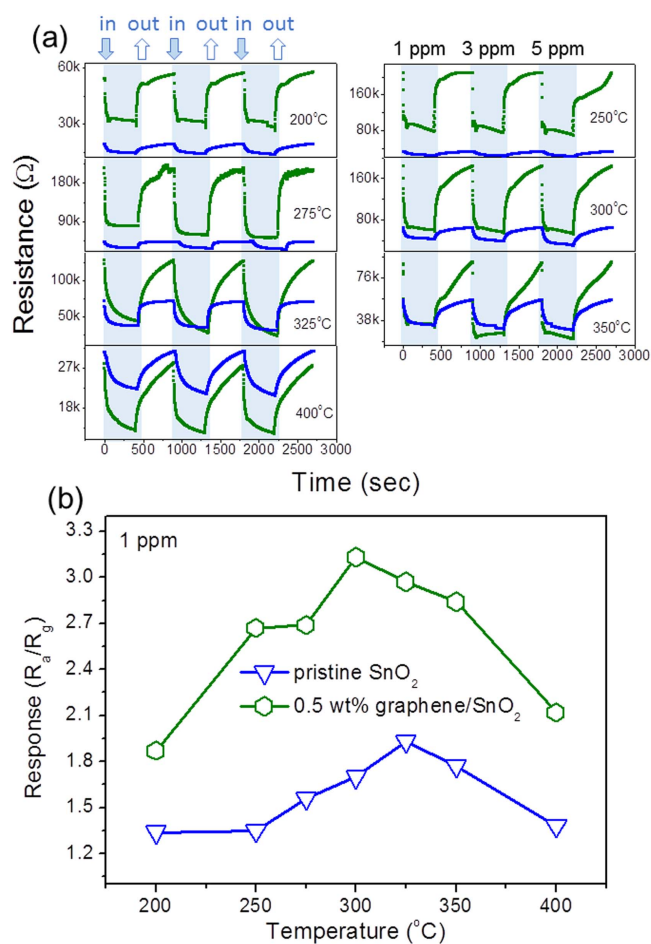
Figure 4. (a) Dynamic resistance curves of the pristine SnO_2 and 0.5 wt% graphene NSs-loaded SnO_2 NFs at various temperatures in the range of 200 °C–400 °C. (b) Summarized responses of pristine SnO_2 and graphene NSs-loaded SnO_2 NFs toward 1 ppm of C_7H_8 as a function of temperature.

concentration was kept very low, ranging from 1 to 5 ppm, as summarized in figure 6. The dynamic resistance curves of pristine SnO_2 and graphene NS-loaded SnO_2 NFs are shown in figures 6(a) and (b), respectively. Figure 6(c) shows the responses of graphene NSs-loaded SnO_2 NFs to 1 ppm of gas relative to the responses of pristine SnO_2 NFs. Graphene NS-loaded SnO_2 NFs showed significantly higher responses than those of pristine SnO_2 NFs. However, significant selectivity towards a particular gas was not observed. This is probably due to the very low concentration of gases. However, analysis of the results revealed that the graphene/SnO_2 sensors were quite selective for H_2S gas at higher concentrations. The response of graphene NS-loaded SnO_2 NFs for 1 ppm of H_2S is 6.46, which is 112.5% higher than that of pristine SnO_2 NFs (figure 6(c), table 1). Moreover, an increase in 134.3% in the response as compared to pristine SnO_2 NFs was observed at 5 ppm of H_2S at the same optimal temperature (table 1). Graphene/SnO_2 sensors showed an H_2S response of 11.6 with an extremely short response time of 3.2 s.

To understand the sensing mechanism of graphene/SnO_2 NFs, we first consider the behaviors of NFs made of n-type materials (such as SnO_2). The higher sensitivity of NFs is

typically attributed to the resistance modulation that arises from the following mechanisms. First, the resistance is modulated along the surface of the NFs. Secondly, the resistance modulation also arises because of potential barriers, which develop at the grain boundaries of the nanograins of NFs. When reducing analytes (e.g., H_2S) are inserted, the reducing gas molecules react with the chemisorbed oxygen at the surface and grain boundaries of the NFs and donate electrons back to the sensor surface. This reduces the potential barriers and increases the conductivity. In the case of H_2S, the pre-adsorbed oxygen is released in the form of H_2O and SO_2 according to the reaction $H_2S_{(g)} + 3O^- \rightarrow SO_{2(g)} + H_2O_{(g)} + 3e^-$. These sensing mechanisms typically operate in n-type metal oxide-based gas sensors with nanofibrous structures. Our experimental results were consistent with the aforementioned mechanism, and the resistance of the pristine SnO_2 NFs decreased upon introduction of reducing gases (e.g., H_2S).

Graphene/SnO_2 heterointerfaces may also be involved in the sensitivity enhancement of graphene NS-loaded SnO_2 NFs (figure 7). In the heterojunctions, the work functions of SnO_2 and graphene are 4.55 and 4.60 eV, respectively [12, 42–44], and the Fermi energy of SnO_2 is lower than that of graphene. Upon the generation of graphene/SnO_2 heterointerfaces, electrons will flow from SnO_2 to graphene, ultimately equilibrating the Fermi level. This charge transfer will form a potential barrier at the heterojunctions, causing the vacuum energy level and the energy band to bend. As a first possibility, the initial transfer of electrons from SnO_2 to graphene will develop a surface depletion region on the SnO_2 surface. As the initial resistance increases, the same change in resistance upon introduction/removal of a target gas will lead to higher sensitivity. As a second possibility, the electrical current across the SnO_2/graphene interfaces will provide an additional change in the resistance. The reducing gases and oxidizing gases will react with adsorbed oxygens, such as O^-, which provide and remove electrons, respectively. Accordingly, reducing and oxidizing gases will decrease and increase the height of potential barriers to electrons, respectively. The reported literature has indicated that the charge flow between different work functions depends on graphene thickness at the interfaces [45]. Ziegler *et al* pointed out that the work function decreases with increasing the number of layers (i.e. thickness) of graphene [46]. By the way, the graphene used in the presetnwork has been exfoliated from the expandable graphite (Hyundai Coma Industry), corresponding to a few-layer graphene. Accordingly, the increase of the graphene content in the graphene NS-loaded SnO_2 NFs will possibly increase the presence of the thicker graphene NSs, resulting in the decrease of the work function of some graphene NSs. If the work function of graphene NSs becomes decreased, the Fermi energy of SnO_2 can be higher than that of graphene. Upon the generation of graphene/SnO_2 heterointerfaces, electrons will flow from graphene to SnO_2, ultimately equilibrating the Fermi level. This charge transfer will form a potential barrier at the heterojunctions, causing the vacuum energy level and the energy band to bend. The initial transfer of electrons from graphene to SnO_2 will not develop a surface depletion region on the SnO_2 surface and will instead
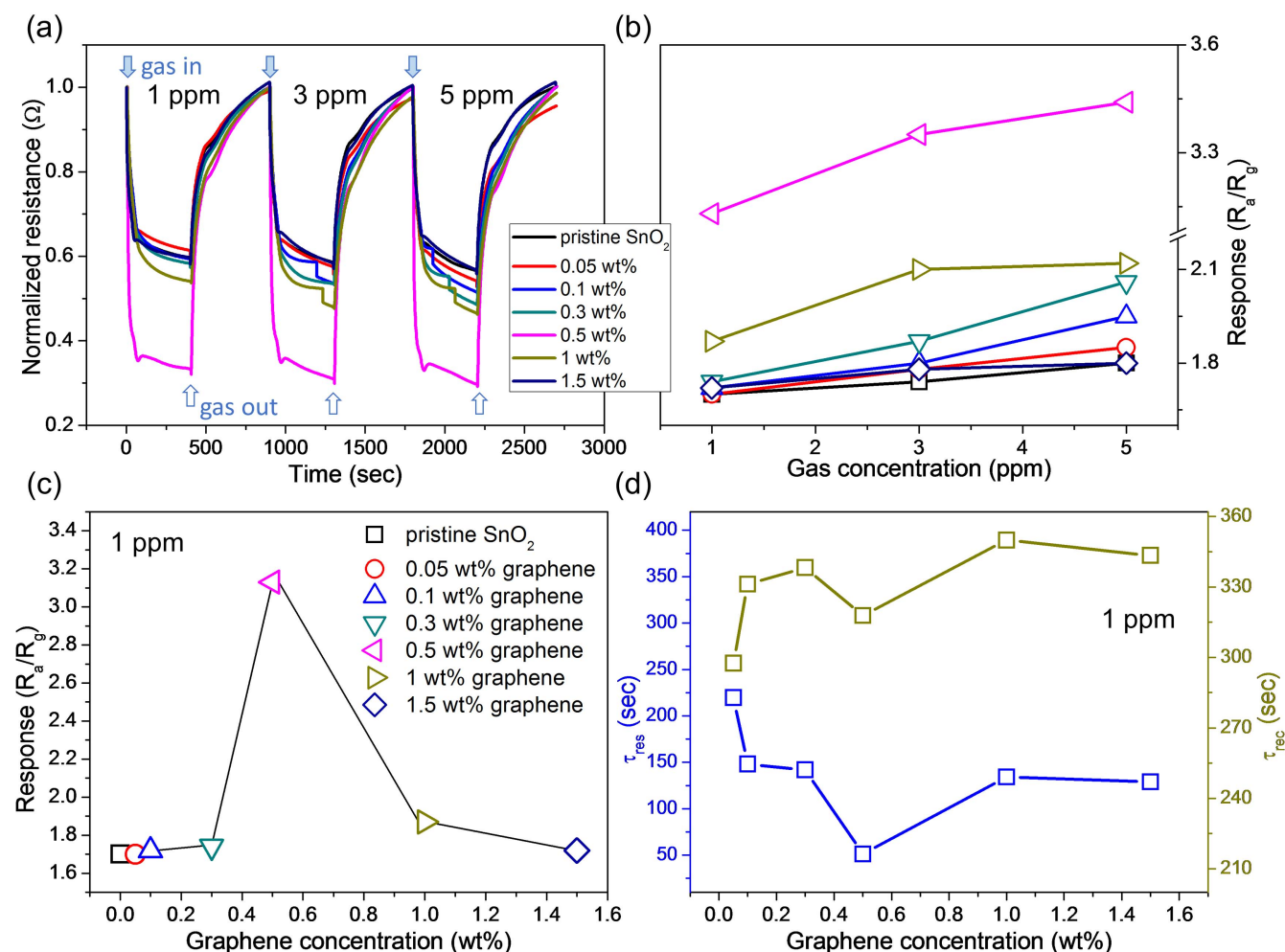
Figure 5. (a) Dynamic resistance curves of the pristine SnO_2 and graphene NSs-loaded SnO_2 NFs with various amounts of graphene (0.05, 0.1, 0.3, 0.5, 1 and 1.5 wt%). The sensing gas was C_7H_8 with concentrations of 1, 3, and 5 ppm, respectively, at 300 °C. (b) Summarized responses as a function of gas concentration. (c) Responses toward 1 ppm of C_7H_8 as a function of graphene content. (d) Response and recovery times for 1 ppm of C_7H_8 at 300 °C.

decrease the resistance. With decreased initial resistance, the modulation of the same amount of resistance, upon the introduction/removal of a target gas, will lead to lower sensitivity. Accordingly, the presence of thicker graphene NS sheets will not favor the enhancement of sensitivity. On the contrary, the presence of thinner graphene NSs is able to enhance the sensitivity. The increase of the graphene content in the graphene NS-loaded SnO_2 NFs will increase the amount of thicker graphene NSs, as well as that of thinner NSs. Accordingly, it is not possible that the change of the graphene content will significantly change the sensor response of the graphene NS-loaded SnO_2 NFs.

In the case of graphene NS-loaded SnO_2 NFs, we first examined the nature and role of graphene NSs in the SnO_2 NFs. The incorporation of graphene led to an increase in the baseline resistance of the pristine SnO_2 NFs, as shown in figure 8. The maximum resistance was obtained by using the optimal amount of graphene (0.5 wt%). This indicates the p-type or electron accepting nature of the graphene in SnO_2 NFs. It also shows that the current flows mainly through interconnected SnO_2 NFs. This observation is consistent with

previous reports [13, 47]. From this, we can also understand the bell-shaped response behavior of graphene NSs-loaded SnO_2 NFs (figure 5(c)). The specific surface area can be another important parameter to affect the sensing properties of NFs with varying graphene NSs content. According to figures 2(a)–(f), the size of the nanograins, the diameter, uniformity and connectivity of the NFs were basically similar, regardless of varying graphene NSs contents, suggesting that microstructure and morphology of individual SnO_2 NFs were not significantly affected by varying the graphene NSs contents in the range of 0.05–1.5 wt%. With these indirect evidences, along with the obvious change of the conductivity of NFs as a function of the graphene NSs content, it is more likely that the conductivity is mainly responsible for the optimum graphene NSs content, in comparison to the influence of the specific surface area.

In the case of low to moderate graphene loadings (0.05–0.5 wt%), conductive graphene NSs dispersed into the NFs, and active interfaces formed between graphene and SnO_2. This increases the sensor resistance and the heights of potential barriers. When a reducing gas was introduced, the
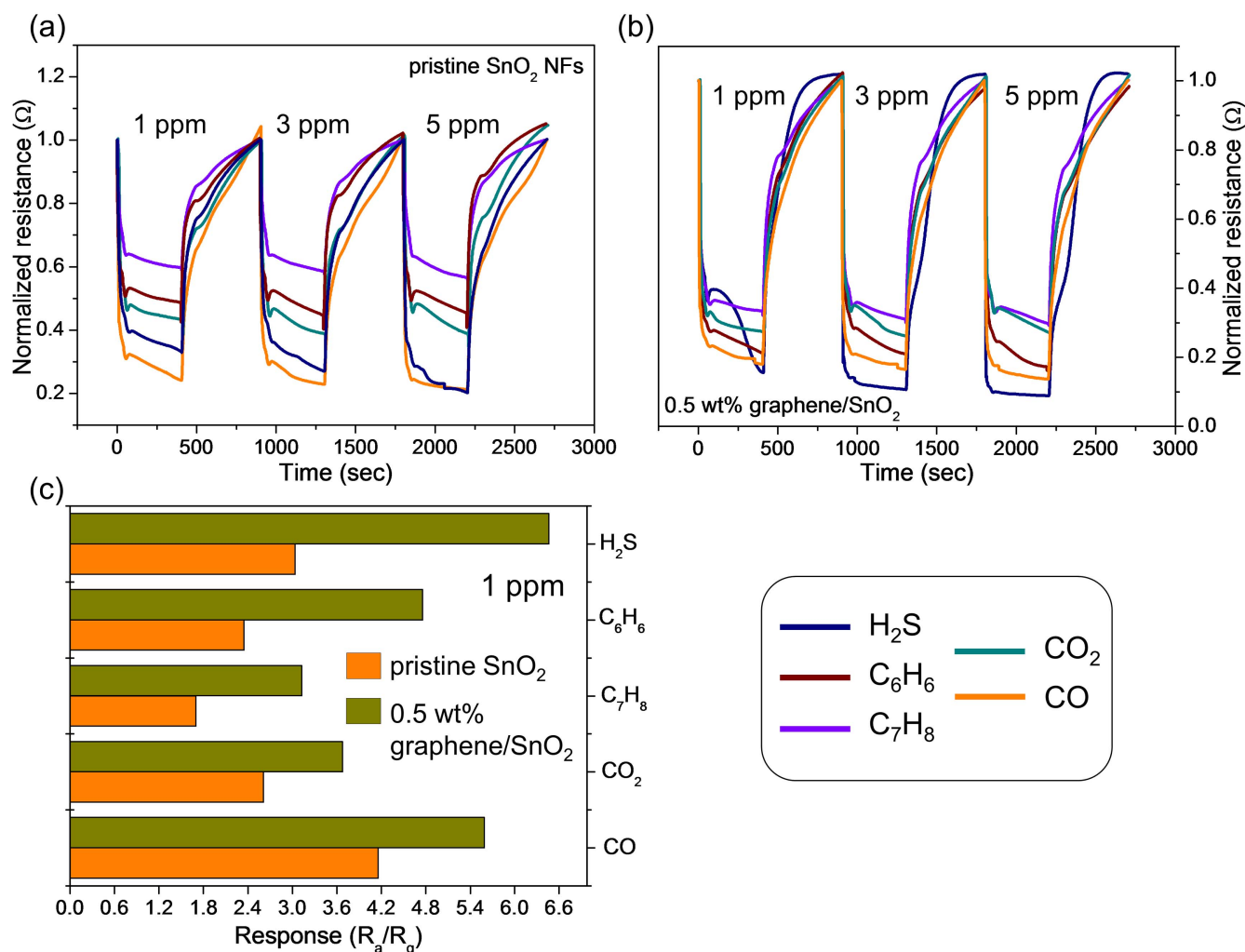
Figure 6. Dynamic resistance curves of (a) pristine SnO$_2$ NFs (b) 0.5 wt% graphene NSs-loaded SnO$_2$ NFs. (c) Summarized responses of the pristine SnO$_2$ and 0.5 wt% graphene NSs-loaded SnO$_2$ NFs for 1 ppm of C$_6$H$_6$, C$_7$H$_8$, CO, CO$_2$, and H$_2$S gases.

Table 1. Sensor responses of the pristine SnO$_2$ and 0.5 wt% graphene NSs-loaded SnO$_2$ NFs for 1 and 5 ppm of C$_6$H$_6$, C$_7$H$_8$, CO, CO$_2$, and H$_2$S gases.

Gas concentration	Pristine SnO$_2$ NFs		0.5 wt% graphene NSs-loaded SnO$_2$ NFs	
	(1 ppm)	(5 ppm)	(1 ppm)	(5 ppm)
CO	4.16	4.79	5.59	7.34
CO$_2$	2.61	2.92	3.68	3.77
C$_7$H$_8$	1.7	1.8	3.13	3.44
C$_6$H$_6$	2.35	2.5	4.76	6.2
H$_2$S	3.04	4.95	6.46	11.6

trapped electrons from the oxygen are released back into the SnO$_2$ NFs; thus, a significant change in the resistance was observed. Alternatively, in the case of loading of high concentrations of graphene, we expected that the overall sensor performance would decrease. First, since the electrical conduction mainly occurs through the SnO$_2$ grains, increasing the graphene content may block electrical currents through SnO$_2$ grains, leading to an increase in the initial resistance. However, this will increase the sensor response (defined as R_a/R_g). Since the initial resistance (R_a) is smaller, the same decrease in resistance caused by the introduction of a reducing gas yields a higher R_a/R_g value. Accordingly, this cannot account for the observed decrease in the sensor response that is caused by increasing the graphene content. Secondly, when a sufficient amount of graphene is provided, graphene NSs begin to connect with each other to provide additional pathways for the flow of electrons. In this case, the flow of electrons occurs mainly through higher conducting pathways along graphene NSs. This will decrease the initial resistance. The same decrease in the resistance caused by the introduction of a reducing gas yields a lower R_a/R_g value, thereby reducing the sensor response. This type of behavior has been reported elsewhere as a function of the graphene concentration [13]. In fact, such behavior has been widely observed when a metal oxide is sensitized by a catalyst or an additive [19, 48]. Therefore, there should be an optimal loading of graphene that achieves high sensing performance in SnO$_2$ NFs. This value was around 0.5 wt% in these experiments. This optimal amount of graphene may seem too small to cause a significant
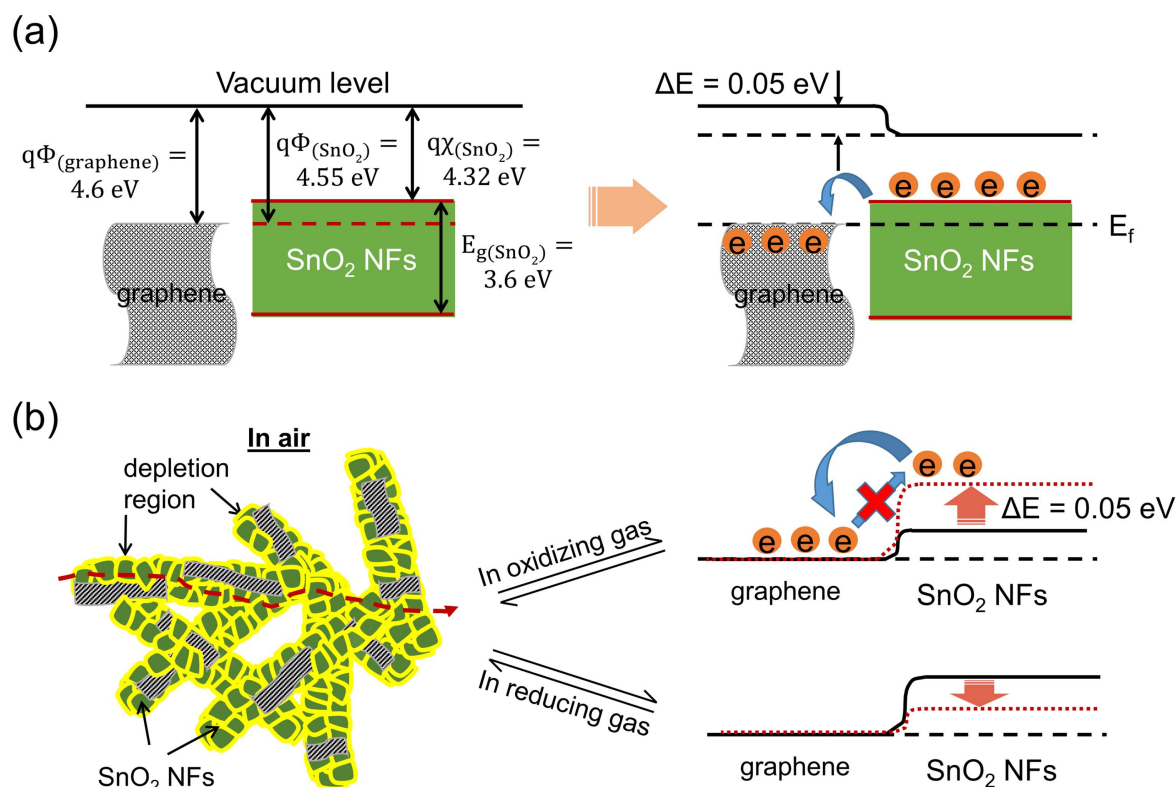
(a)

(b)

Figure 7. Schematic illustration of the sensing mechanism of graphene NSs-loaded SnO_2 NFs.
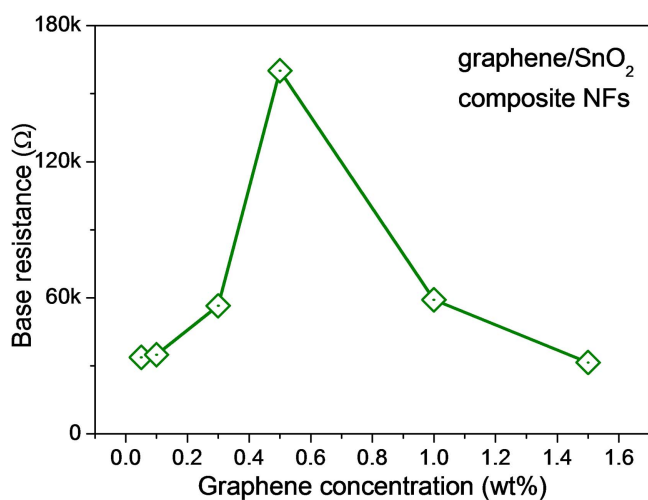

Figure 8. Variation of the baseline resistance of the graphene NSs-loaded SnO_2 NFs sensor, by varying the graphene concentration.

change, but the actual volume and number of graphene NSs incorporated are very large due to the very small density of graphene. Thus, there are a large number of graphene/SnO_2 heterointerfaces, which have a significant effect on the resistance modulation of SnO_2 NFs.

4. Conclusions

We compared the gas sensing characteristics of graphene NS-loaded SnO_2 NFs and pristine SnO_2 NFs at very low concentrations of C_6H_6, C_7H_8, CO, CO_2, and H_2S at various temperatures ranging from 200 °C to 400 °C. FE-SEM and HR-TEM analyses confirmed the presence of graphene NSs and revealed the nature of their interaction with the nanograins of the polycrystalline SnO_2 NFs. The optimal amount of graphene and the optimum operating temperature were observed to be 0.5 wt% and 300 °C, respectively. The loading of graphene NSs into SnO_2 NFs enhanced the sensitivity and lowered the optimal operating temperature of the SnO_2 NFs. The optimized graphene NS-loaded SnO_2 NFs exhibited sensor responses of 6.46 and 11.6 at 1 and 5 ppm of H_2S gas, respectively. These sensors also showed an extremely short response time of 3.2 s at 5 ppm of H_2S gas. Apart from the modulated resistance along the surface and in the grain boundaries of the nanograins in the SnO_2 NFs, the enhanced sensing capabilities caused by the incorporation of graphene NSs were ascribed to a variety of mechanisms. These include the catalytic effects of graphene and the generation of SnO_2/graphene heterointerfaces. Since graphene NS-loaded SnO_2 NFs showed excellent sensitivity towards very low concentrations (1–5 ppm) of gases, graphene-loaded SnO_2 NFs are potential candidates for next-generation gas sensors.

References

[1] Zhang J, Liu X, Neri G and Pinna N 2016 Nanostructured materials for room-temperature gas sensors *Adv. Mater.* **28** 795–831

[2] Neri G 2015 First fifty years of chemoresistive gas sensors *Chemosensors* **3** 1–20

[3] Zhou X, Lee S, Xu Z and Yoon J 2015 Recent progress on the development of chemosensors for gases *Chem. Rev.* **115** 7944–8000

[4] Luo C J, Stoyanov S D, Stride E, Pelan E and Edirisinghe M 2012 Electrospinning versus fibre production methods: from specifics to technological convergence *Chem. Soc. Rev.* **41** 4708–35

[5] Landau O, Rothschild A and Zussman E 2009 Processing-microstructure-properties correlation of ultrasensitive gas sensors produced by electrospinning *Chem. Mater.* **21** 9–11

[6] Lu X, Wang C and Wei Y 2009 One-dimensional composite nanomaterials: synthesis by electrospinning and their applications *Small* **5** 2349–70

[7] Ramesh Kumar P, Khan N, Vivekanandhan S, Satyanarayana N, Mohanty A K and Misra M 2012 Nanofibers: effective generation by electrospinning and their applications *J. Nanosci. Nanotechnol.* **12** 1–25

[8] Yang D J, Kamienchick I, Youn D Y, Rothschild A and Kim I D 2010 Ultrasensitive and highly selective gas sensors based on electrospun SnO_2 nanofibers modified by Pd loading *Adv. Funct. Mater.* **20** 4258–64

[9] Dong K Y *et al* 2011 Enhanced H_2S sensing characteristics of Pt doped SnO_2 nanofibers sensors with micro heater *Sensors Actuators* B **157** 154–61

[10] Zhao Y, He X L, Li J P, Gao X G and Jia J 2012 Porous CuO/SnO_2 composite nanofibers fabricated by electrospinning and their H_2S sensing properties *Sensors Actuators* B **165** 82–7

[11] Wang Z J *et al* 2010 Improved hydrogen monitoring properties based on p-NiO/n-SnO_2 heterojunction composite nanofibers *J. Phys. Chem.* C **114** 6100–5

[12] Lee J H, Katoch A, Choi S W, Kim J H, Kim H W and Kim S S 2015 Extraordinary improvement of gas-sensing performances in SnO_2 nanofibers due to creation of local p–n heterojunctions by loading reduced graphene oxide nanosheets *ACS Appl. Mater. Inter.* **7** 3101–9

[13] Tammanoon N *et al* 2015 Ultrasensitive NO_2 sensor based on ohmic metal-semiconductor interfaces of electrolytically exfoliated graphene/flame-spray-made SnO_2 nanoparticles composite operating at low temperatures *ACS Appl. Mater. Interfaces* **7** 24338–52

[14] Choi S J, Jang B H, Lee S J, Min B K, Rothschild A and Kim I D 2014 Selective detection of acetone and hydrogen sulfide for the diagnosis of diabetes and halitosis using SnO_2 nanofibers functionalized with reduced graphene oxide nanosheets *ACS Appl. Mater. Interfaces* **6** 2588–97

[15] Moon S *et al* 2016 Co_3O_4-SWCNT composites for H_2S gas sensor application *Sensors Actuators* B **222** 166–72

[16] Choi S J *et al* 2015 Highly efficient electronic sensitization of non-oxidized graphene flakes on controlled pore-loaded WO_3 nanofibers for selective detection of H_2S molecules *Sci. Rep.* **5** 8067–76

[17] Kong J *et al* 2000 Nanotube molecular wires as chemical sensors *Science* **287** 622–5

[18] Abideen Z U, Kim H W and Kim S S 2015 An ultra-sensitive hydrogen gas sensor using reduced graphene oxide-loaded ZnO nanofibers *Chem. Commun.* **51** 15418–21

[19] Abideen Z U, Katoch A, Kim J H, Kwon Y J, Kim H W and Kim S S 2015 Excellent gas detection of ZnO nanofibers by loading with reduced graphene oxide nanosheets *Sensors Actuators* B **221** 1499–507

[20] Gadipelli S and Guo Z X 2015 Graphene-based materials: synthesis and gas sorption, storage and separation *Prog. Mater. Sci.* **69** 1–60

[21] Van den Brink J 2007 Graphene: from strength to strength *Nat. Nanotechnol.* **2** 199–201

[22] Schedin F *et al* 2007 Detection of individual gas molecules adsorbed on graphene *Nat. Mater.* **6** 652–5

[23] Drewniak S, Muzyka R, Stolarczyk A, Pustelny T, Kotyczka-Moranska M and Setkiewicz M 2016 Studies of reduced graphene oxide and graphite oxide in the aspect of their possible application in gas sensors *Sensors* **16** 103

[24] Bo Z *et al* 2014 Green preparation of reduced graphene oxide for sensing and energy storage applications *Sci. Rep.* **4** 4684–92

[25] Yuan W J and Shi G Q 2013 Graphene-based gas sensors *J. Mater. Chem.* A **1** 10078–91

[26] Gupta Chatterjee S, Chatterjee S, Ray A K and Chakraborty A K 2015 Graphene-metal oxide nanohybrids for toxic gas sensor: a review *Sensors Actuators* B **221** 1170–81

[27] Varghese S S, Lonkar S, Singh K K, Swaminathan S and Abdala A 2015 Recent advances in graphene based gas sensors *Sensors Actuators* B **218** 160–83

[28] Kulkarni G S, Reddy K, Zhong Z and Fan X 2014 Graphene nanoelectronic heterodyne sensor for rapid and sensitive vapour detection *Nat. Commun.* **5** 4376–83

[29] Van Khai T *et al* 2012 Significant enhancement of blue emission and electrical conductivity of N-doped graphene *J. Mater. Chem.* **22** 17992

[30] Hummers W S and Offeman R E 1958 Preparation of graphitic oxide *J. Am. Chem. Soc.* **80** 1339–1339

[31] Choi S W, Park J Y and Kim S S 2009 Synthesis of SnO_2–ZnO core–shell nanofibers via a novel two-step process and their gas sensing properties *Nanotechnology* **20** 465603

[32] Stankovich S, Dikin D A, Piner R D, Kohlhaas K A, Kleinhammes A, Jia Y, Wu Y, Nguten S T and Ruoff R S 2007 Synthesis of graphene-based nanosheets via chemical reduction of exfoliated graphite oxide *Carbon* **45** 1558–65

[33] Cui P, Lee J, Hwang E and Lee H 2011 One-pot reduction of graphene oxide at subzero temperatures *Chem. Commun.* **47** 12370–2

[34] Park J Y, Choi S W and Kim S S 2009 Fabrication of a highly sensitive chemical sensor based on ZnO nanorod arrays *Nanoscale Res. Lett.* **5** 353–9

[35] Park J Y, Choi S W, Lee J W, Lee C and Kim S S 2009 Synthesis and gas sensing properties of TiO_2–ZnO core–shell nanofibers *J. Am. Ceram. Soc.* **92** 2551–4

[36] Yamazoe N, Sakai G and Shimanoe K 2003 Oxide semiconductor gas sensors *Catal. Surv. Asia* **7** 63–75

[37] Malyshev V V and Pislyakov A V 2008 Investigation of gas-sensitivity of sensor structures to hydrogen in a wide range of temperature, concentration and humidity of gas medium *Sensors Actuators* B **134** 913–21

[38] Cao M, Wang Y, Chen T, Antonietti M and Niederberger M 2008 A highly sensitive and fast-responding ethanol sensor based on $CdIn_2O_4$ nanocrystals synthesized by a nonaqueous sol–gel route *Chem. Mater.* **20** 5781–6

[39] Kim J H, Katoch A, Kim H W and Kim S S 2016 Realization of ppm-level CO detection with exceptionally high sensitivity using reduced graphene oxide-loaded SnO_2 nanofibers with simultaneous Au functionalization *Chem. Commun.* **52** 3832–5

[40] Kozhushner M A, Trakhtenberg L I, Bodneva V L, Belisheva T V, Landerville A C and Oleynik I I 2014 Effect of temperature and nanoparticle size on sensor properties of nanostructured tin dioxide films *J. Phys. Chem.* C **118** 11440–4

[41] Liu C Y, Chen C F, Leu J P, Lu C C and Liao K H 2009 Fabrication and carbon monoxide sensing characteristics of mesostructured carbon gas sensors *Sensors Actuators* B **143** 12–6

[42] Zhang D, Xie F, Lin P and Choy W C 2013 Al-TiO$_2$ composite-modified single-layer graphene as an efficient transparent cathode for organic solar cells *ACS Nano* **7** 1740–7

[43] Li S S, Tu K H, Lin C C, Chen C W and Chhowalla M 2010 Solution-processable graphene oxide as an efficient hole transport layer in polymer solar cells *ACS Nano* **4** 3169–74

[44] Song S M, Park J K, Sul O J and Cho B J 2012 Determination of work function of graphene under a metal electrode and its role in contact resistance *Nano Lett.* **12** 3887–92

[45] Kuo C C and Chen C H 2014 Graphene thickness-controlled photocatalysis and surface enhanced Raman scattering *Nanoscale* **6** 12805

[46] Ziegler D, Gava P, Güttinger J, Moliter F, Wirtz L, Lazzeri M, Saitta A M, Stemmer A, Mauri F and Stamper C 2011 Variations in the work function of doped single- and few-layer graphene assessed by Kelvin probe force microscopy and density functional theory *Phys. Rev.* B **83** 235434

[47] Ratinac K R, Yang W, Ringer S P and Braet F 2010 Toward ubiquitous environmental gas sensors-capitalizing on the promise of graphene *Environ. Sci. Technol.* **44** 1167–76

[48] Ding J, Zhu J W, Yao P C, Li J, Bi H P and Wang X 2015 Synthesis of ZnO–Ag hybrids and their gas-sensing performance toward ethanol *Ind. Eng. Chem. Res.* **54** 8947–53